Journal of Computational Physics 229 (2010) 7893–7910

Contents lists available at ScienceDirect

Journal of Computational Physics

journal homepage: www.elsevier.com/locate/jcp

A fourth-order divergence-free method for MHD flows

Shengtai Li *

Theoretical Division, MS B284, Los Alamos National Laboratory, Los Alamos, NM 87545, United States

ARTICLE INFO

Article history:
Received 18 February 2010
Received in revised form 24 June 2010
Accepted 30 June 2010
Available online 6 July 2010

Keywords:
Finite-volume method
Central schemes
High order
Non-oscillatory
Constrained transport (CT)
Divergence-free reconstruction
Overlapping cell
Magneto-hydrodynamics (MHD)
Turbulence

ABSTRACT

This paper extends our previous third-order method [S. Li, High order central scheme on overlapping cells for magneto-hydrodynamic flows with and without constrained transport method, J. Comput. Phys. 227 (2008) 7368–7393] to the fourth-order. Central finite-volume schemes on overlapping grid are used for both the volume-averaged variables and the face-averaged magnetic field. The magnetic field at the cell boundaries falls within the dual grid and is naturally continuous so that our method eliminates the instability triggered by the discontinuity in the normal component of the magnetic field. Our fourth-order scheme has much smaller numerical dissipation than the third-order scheme. The divergence-free condition of the magnetic field is preserved by our fourth-order divergence-free reconstruction and the constrained transport method. Numerical examples show that the divergence-free condition is essential to the accuracy of the method when a limiter is used in the reconstruction. The high-order, low-dissipation, and divergence-free properties of this method make it an ideal tool for direct magneto-hydrodynamic turbulence simulations.

Published by Elsevier Inc.

1. Introduction

In a previous paper [1], we described a third-order divergence-free central scheme on overlapping cells for magneto-hydrodynamic (MHD) flows. The divergence-free condition of the magnetic field is preserved locally by the constrained transport (CT) method [2]. The CT method uses a staggered approach and demands calculation of the electro-motive force (EMF) at the cell corners (2D) or cell edges (3D). For Godunov methods using a single grid, the EMF is usually calculated as the flux at cell faces and then a spatial averaging (e.g., [3]) or interpolation (e.g., [4]) is used to obtain the EMF at the staggered position. The overlapping cells provide a natural way to calculate EMF using high-order method without spatial averaging or interpolations (see [1]). The overlapping cells also naturally preserve the continuity of the normal component of the magnetic field at the cell faces so that our schemes do not suffer from the instability described in [5].

The extension of the third-order central scheme of Liu et al. [6] to the fourth-order scheme for the cell volume-averaged variables is straightforward. Although the least-square reconstruction method proposed in [6] can be used in any high-order method, it is more expensive than the method that uses less information around the cell. Since the reconstruction is used in every stage of a Runge–Kutta method in a time integration, we propose a simplified fourth-order reconstruction to reduce the computational cost.

We also extend our third-order divergence-free reconstruction [1] to the fourth-order method. Unlike the third-order method, the available reconstruction information from the cell faces is not sufficient to determine a fourth-order divergence-free reconstructed polynomial over the whole cell. An additional constraint from nearby cells is needed.

* Tel.: +1 505 665 8407.
E-mail address: sli@lanl.gov

0021-9991/$ - see front matter Published by Elsevier Inc.
doi:10.1016/j.jcp.2010.06.044

For MHD flows that contain shock and contact discontinuity, we use an essentially-non-oscillatory (ENO) reconstruction to preserve the monotonicity of the fluid variables. This limited reconstruction uses only adjacent nearest neighbor via a hierarchical procedure (see [6]) to keep the stencil compact. To reduce the overshoots/undershoots near the discontinuities, we adopt a new technique proposed in Liu et al. [7], which lowers the order of the remainder of polynomial in the current cell during the hierarchical reconstruction.

As noted in our previous paper [1], the divergence error of the magnetic field in central schemes without CT is relatively smaller than that in the upwind-type schemes. Most of problems can be solved quite well without the divergence-free constraint. However, this conclusion is no longer true for the fourth-order method. Our numerical examples show that if a limiter, which is required for problems involving the discontinuities, is used in the reconstruction, the divergence error of the fourth-order method increases dramatically such that it not only degenerates the accuracy of the method but also can break down the simulations.

The outline of the paper is as follows: In Section 3, we review the central schemes on overlapping cells and propose a fourth-order central scheme for both the volume-averaged variables and the face-centered magnetic field. In Section 4, we derive a fourth-order divergence-free reconstruction. Several examples are given in Section 5, demonstrating the effectiveness of our scheme.

2. Ideal MHD equations

The ideal MHD equations in conservative form can be written as

$$\begin{aligned}
&\rho_t + \nabla\cdot(\rho\mathbf{v}) = 0,\\
&(\rho\mathbf{v})_t + \nabla\cdot\left[\rho\mathbf{v}\mathbf{v}^T + p\mathbf{I} - \mathbf{B}\mathbf{B}^T\right] = 0,\\
&\mathbf{B}_t - \nabla\cdot\left(\mathbf{v}\mathbf{B}^T - \mathbf{B}\mathbf{v}^T\right) = 0,\\
&E_t + \nabla\cdot[(E+p)\mathbf{v} - \mathbf{B}(\mathbf{v}\cdot\mathbf{B})] = 0,
\end{aligned} \tag{1}$$

where ρ is density, $\mathbf{v}$ is the velocity, $\mathbf{B}$ is the magnetic field, $\mathbf{I}$ is the 3×3 unit tensor, E is the total energy per unit volume, and $p = p_{\text{gas}} + \mathbf{B}\cdot\mathbf{B}/2$ is the total pressure, where p_{gas} is the gas pressure that satisfies the equation of state,

$$p_{\text{gas}} = (\gamma-1)\left(E - \frac{1}{2}\rho\mathbf{v}\cdot\mathbf{v} - \frac{1}{2}\mathbf{B}\cdot\mathbf{B}\right),$$

and γ is the adiabatic index for the ideal plasma. One external constraint for magnetic field is the *divergence-free* condition $\nabla\cdot\mathbf{B} = 0$.

Generally, the induction equation for the magnetic field can be written as

$$\frac{\partial\mathbf{B}}{\partial t} = -\nabla\times\mathbf{E}, \tag{2}$$

where the electro-motive force $\mathbf{E}$ is defined as $\mathbf{E} = -\mathbf{v}\times\mathbf{B} + \eta\mathbf{J}$, $\mathbf{J} = \nabla\times\mathbf{B}$ is the current density, η is the resistivity. For ideal MHD, $\eta = 0$. From now on, we will consider only the ideal MHD in this paper.

To preserve the divergence-free condition of the magnetic field, we adopt the constrained transport approach [2,8,9,3,10,11], which uses the staggered grid and treats the magnetic field as the face-centered area-averaged variables and other fluid quantities (e.g., density, momentum, pressure and total energy) as the cell-centered volume-averaged variables.

3. Central schemes on overlapping cells

3.1. Central schemes for the volume-averaged variables

For the sake of a self-contained presentation we summarize the central scheme presented by Liu et al. [6]. Denote the cell-centered variables as $\mathbf{u}$, and rewrite their equations as a system of conservation law

$$\frac{\partial\mathbf{u}}{\partial t} + \nabla\cdot\mathbf{F}(\mathbf{u}) = 0. \tag{3}$$

For simplicity, we assume a uniform staggered rectangular mesh depicted in Fig. 1 for the 2D case. Let $\{C_{I+1/2}\}$, $I = i,j$ be a partition of R^2 into uniform square cells depicted by solid lines in Fig. 1 and tagged by their cell centroids at the half integers, $\mathbf{x}_{I+1/2} := (I+1/2)\Delta x$. Let $\overline{U}_{I+1/2}(t)$ be the numerical cell average approximating $(1/|C_{I+1/2}|)\int_{C_{I+1/2}} u(\mathbf{x},t)d\mathbf{x}$, in particular, $\overline{U}^n_{I+1/2} = \overline{U}_{I+1/2}(t^n)$. We will denote these cells as U-cell subsequently. Let $\{D_I\}$ be the dual mesh which consists of a $\Delta x/2$-shift of the $C_{I+1/2}$'s depicted by dash lines in Fig. 1. Let $\mathbf{x}_I$ be the cell centroid of the cell D_I. Let $V_I(t)$ be the numerical cell average approximating $(1/|D_I|)\int_{D_I} u(\mathbf{x},t)d\mathbf{x}$. We will refer these cells as V-cells. The semi-discrete central scheme on overlapping cells can be written as follows (for detailed derivation, see [12,6]):

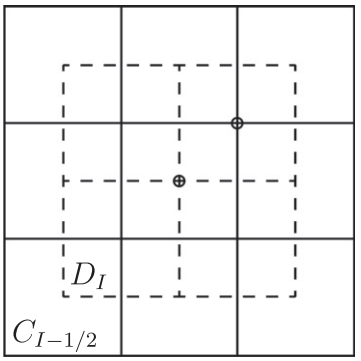

Fig. 1. Illustration of the overlapping cells. Both the primal grid (solid line) and the overlapping grid (dashed line) cover the whole domain.

$$\frac{d}{dt}\overline{U}_{I+\frac{1}{2}}(t^n) = \frac{1}{\Delta\tau^n}\left(\frac{1}{|C_{I+\frac{1}{2}}|}\int_{C_{I+\frac{1}{2}}} V^n(\mathbf{x})d\mathbf{x} - \overline{U}^n_{I+\frac{1}{2}}\right) - \frac{1}{|C_{I+\frac{1}{2}}|}\int_{\partial C_{I+\frac{1}{2}}} \mathbf{f}(V^n(\mathbf{x}))\cdot\mathbf{n}\,ds, \tag{4}$$

$$\frac{d}{dt}\overline{V}_I(t^n) = \frac{1}{\Delta\tau^n}\left(\frac{1}{|D_I|}\int_{D_I} U^n(\mathbf{x})d\mathbf{x} - \overline{V}^n_I\right) - \frac{1}{|D_I|}\int_{\partial D_I} \mathbf{f}(U^n(\mathbf{x}))\cdot\mathbf{n}\,ds, \tag{5}$$

where $\Delta\tau^n$ is a parameter dictated by the CFL condition ($\Delta\tau^n$ = (CFL factor) $\times$ Δx/(maximum characteristic speed)), $U^n(\mathbf{x})$ and $V^n(\mathbf{x})$ are higher-order piecewise polynomial approximation on cells $C_{I+1/2}$ and D_I, respectively. The actually time step-size, Δt, can be much smaller than $\Delta\tau$ for convection–diffusion equations. The introduction of $\Delta\tau$ avoids the $O(1/\Delta t)$ dependence of the dissipation (see [12]) when $\Delta t \to 0$.

To achieve the fourth-order accuracy, the volume integrals on the right-hand side of Eqs. (4) and (5) are obtained by integrating a fourth-order reconstruction polynomial exactly, and the face integrals of the flux are calculated by the two-point Gaussian quadrature rule.

3.2. The fourth-order reconstruction for the cell-centered variables over the cell

The fourth-order reconstruction in cell $C_{J-1/2}$ (see Fig. 1) can be represented by a cubic polynomial in 2D,

$$\begin{aligned} u(x-x_i,y-y_j) = {} & u_0(0,0) + u_x(0,0)(x-x_i) + u_y(0,0)(y-y_j) + \frac{1}{2}u_{xx}(0,0)(x-x_i)^2 + u_{xy}(0,0)(x-x_i)(y-y_j) \\ & + \frac{1}{2}u_{yy}(0,0)(y-y_j)^2 + \frac{1}{6}u_{xxx}(0,0)(x-x_i)^3 + \frac{1}{2}u_{xxy}(0,0)(x-x_i)^2(y-y_j) + \frac{1}{2}u_{xyy}(0,0)(x-x_i)(y-y_j)^2 \\ & + \frac{1}{6}u_{yyy}(0,0)(y-y_j)^3, \end{aligned} \tag{6}$$

where (x_i,y_j) is the cell centroid of the cell $C_{J-1/2}$, and the 10 coefficients, $u_0, u_x, \ldots, u_{yyy}$, are to be determined by the known cell-averaged quantities.

Liu et al. [6] described a fourth-order reconstruction in 2D for the volume-averaged quantities using a least-square approach. It uses 13 cells (see Fig. 2) to construct a cubic polynomial with 10 coefficients. Using numerical experiments, we have found that the cost of the fourth-order reconstruction (without limiting) is roughly 70% of the total simulation time. This is because a dense matrix–vector product ($A_{10,13}V_{13}$) must be performed for each reconstructed cell.

To improve the computational efficiency without loss of the accuracy, we propose to use a different reconstruction method. Instead of picking a suitable set of 10 cells, we still use the 13 cells as depicted in Fig. 2. The fourth-order accurate derivatives for cell C_7 can be derived easily as follows:

$$u_{xx} = \frac{\bar{u}_8 - 2\bar{u}_7 + \bar{u}_6}{\Delta^2 x},$$

$$u_{yy} = \frac{\bar{u}_2 - 2\bar{u}_7 + \bar{u}_{12}}{\Delta^2 x},$$

$$u_{xxy} = \frac{(\bar{u}_1 - 2\bar{u}_2 + \bar{u}_3) - (\bar{u}_{11} - 2\bar{u}_{12} + \bar{u}_{13})}{\Delta^2 x(2\Delta y)},$$

$$u_{xyy} = \frac{(\bar{u}_3 - 2\bar{u}_8 + \bar{u}_{13}) - (\bar{u}_1 - 2\bar{u}_6 + \bar{u}_{11})}{\Delta^2 y(2\Delta x)}.$$

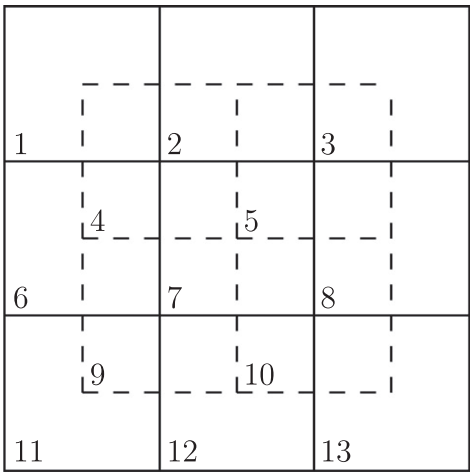

Fig. 2. Construction of a cubic polynomial for cell C_7 using the nearby 13 cells, The dashed line cells are *V*-cell.

From u_{xx} and u_{yy}, we can obtain

$$u_0 = \bar{u}_7 - \frac{1}{24}(u_{xx}\Delta^2 x + u_{yy}\Delta^2 y).$$

The mixed derivative u_{xy} can be calculated using two sets of cells: $(1,3,11,13)$ and $(4,5,9,10)$. We choose the more compact one, which is $(4,5,9,10)$, to construct the u_{xy},

$$u_{xy} = \frac{\bar{v}_5 + \bar{v}_9 - \bar{v}_4 - \bar{v}_{10}}{\Delta x \Delta y}.$$

The estimation of the third-order derivatives u_{xxx} and u_{yyy} is a bit more complicated. It requires both *U*-cell and *V*-cell. After manipulations using the volume integrals over each cell, we obtain

$$u_{xxx} = \frac{u_{xyy} + 4[\bar{u}_8 - (\bar{v}_5 + \bar{v}_{10}) + (\bar{v}_4 + \bar{v}_9) - \bar{u}_6]}{\Delta^3 x},$$
$$u_{yyy} = \frac{u_{xxy} + 4[\bar{u}_2 - (\bar{v}_5 + \bar{v}_4) + (\bar{v}_{10} + \bar{v}_9) - \bar{u}_{12}]}{\Delta^3 y}.$$

Finally, the first derivatives can be easily computed with the known information

$$u_x = \frac{\bar{u}_8 - \bar{u}_6}{2\Delta x} - \frac{1}{24}u_{xyy} - \frac{5}{24}u_{xxx},$$
$$u_y = \frac{\bar{u}_2 - \bar{u}_{12}}{2\Delta y} - \frac{1}{24}u_{xxy} - \frac{5}{24}u_{yyy}.$$

We have verified that the reconstruction polynomial using the above reconstructed derivatives and coefficients is of fourth-order accuracy. It can be verified easily that our 2D reconstruction will reduce to the 1D reconstruction for planar, grid-aligned flows. With the reduced formulation of the derivatives, the computation of the reconstruction reduces to 30% of the total cost.

3.3. The fourth-order central schemes for the face-centered magnetic field

The constrained transport (CT) schemes are built upon area-averaged magnetic field components located at the faces of a grid cell. The components of the area-averaged magnetic field are placed at different faces. For a 2D example and cell $C_{i+1/2,j+1/2}$, the B_x component is defined as

$$\bar{b}^U_{x,i,j+1/2} = \frac{1}{\Delta y}\int_{y_j}^{y_{j+1}} B^U_x(x_i, y)dy, \tag{7}$$

where the superscript U in B^U_x is used to indicate that the solution is for the *U*-cells, the lower case b is used to indicate that this is a face-centered component of the magnetic field while the upper case B is used for the volume-averaged cell-centered component of the magnetic field. Analogous expressions can be written down for $\bar{b}^U_{y,i+1/2,j}$. The collocation of variables is illustrated in Fig. 3. The overlapping cells D_I provide more information for the collocated components of the magnetic field, since each face of the D_I is orthogonal to a face of $C_{I+1/2}$ at the face center. For a 2D problem, the location of the cell-centered magnetic field B of D_I is exactly the same as the location of the electric field E of $C_{I+1/2}$.

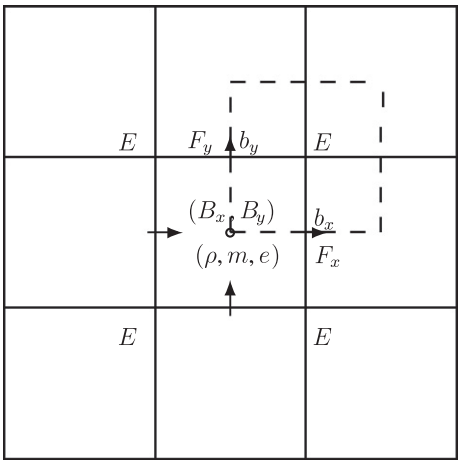

Fig. 3. Illustration of the staggered grid and the collocation of the magnetic field. The electrical field E is located at the cell corner. The magnetic field b_x and b_y, and flux F_x and F_y are located at the face center. The other fluid variables and cell-centered magnetic field B_x and B_y are located at the cell center.

The central schemes for the face-centered magnetic field in a 2D grid are

$$\frac{d}{dt}\bar{b}^U_{x,i,j+\frac{1}{2}}(t^n) = \frac{1}{\Delta\tau^n}\left(\frac{1}{\Delta y}\int_{y_j}^{y_{j+1}} b_x^{V^n}(x_i,y)dy - \bar{b}^{U^n}_{x,i,j+\frac{1}{2}}\right) - \frac{E^V_{z,i,j+1} - E^V_{z,i,j}}{\Delta y}, \tag{8}$$

$$\frac{d}{dt}\bar{b}^U_{y,i+\frac{1}{2},j}(t^n) = \frac{1}{\Delta\tau^n}\left(\frac{1}{\Delta x}\int_{x_i}^{x_{i+1}} b_y^{V^n}(x,y_j)dx - \bar{b}^{U^n}_{y,i+\frac{1}{2},j}\right) + \frac{E^V_{z,i+1,j} - E^V_{z,i,j}}{\Delta x}, \tag{9}$$

$$\frac{d}{dt}\bar{b}^V_{x,i+\frac{1}{2},j}(t^n) = \frac{1}{\Delta\tau^n}\left(\frac{1}{\Delta y}\int_{y_{j-\frac{1}{2}}}^{y_{j+\frac{1}{2}}} b_x^{U^n}\left(x_{i+\frac{1}{2}},y\right)dy - \bar{b}^{V^n}_{x,i+\frac{1}{2},j}\right) - \frac{E^U_{z,i+\frac{1}{2},j+\frac{1}{2}} - E^U_{z,i+\frac{1}{2},j-\frac{1}{2}}}{\Delta y}, \tag{10}$$

$$\frac{d}{dt}\bar{b}^V_{y,i,j+\frac{1}{2}}(t^n) = \frac{1}{\Delta\tau^n}\left(\frac{1}{\Delta x}\int_{x_{i-\frac{1}{2}}}^{x_{i+\frac{1}{2}}} b_y^{U^n}\left(x,y_{i+\frac{1}{2}}\right)dx - \bar{b}^{V^n}_{y,i,j+\frac{1}{2}}\right) + \frac{E^U_{z,i+\frac{1}{2},j+\frac{1}{2}} - E^U_{z,i-\frac{1}{2},j+\frac{1}{2}}}{\Delta x}. \tag{11}$$

Note that the accuracy of the schemes depends only on the order of the reconstruction polynomial.

3.4. The divergence-free reconstruction over a cell

To achieve the fourth-order accuracy overall, we must have a fourth-order divergence-free reconstruction for the magnetic field. For the 2D Cartesian grid, the cubic reconstructed polynomials can be written as

$$\begin{aligned} B_x(x,y) &= a_0 + a_1x + a_2y + \frac{1}{2}a_{11}x^2 + a_{12}xy + \frac{1}{2}a_{22}y^2 \\ &\quad + \frac{1}{6}a_{111}x^3 + \frac{1}{2}a_{112}x^2y + \frac{1}{2}a_{122}xy^2 + \frac{1}{6}a_{222}y^3, \end{aligned} \tag{12}$$

$$\begin{aligned} B_y(x,y) &= b_0 + b_1x + b_2y + \frac{1}{2}b_{11}x^2 + b_{12}xy + \frac{1}{2}b_{22}y^2 \\ &\quad + \frac{1}{6}b_{111}x^3 + \frac{1}{2}b_{112}x^2y + \frac{1}{2}b_{122}xy^2 + \frac{1}{6}b_{222}y^3, \end{aligned} \tag{13}$$

where subscript "1" denotes the derivative with respect to x and subscript "2" denotes the derivative with respect to y in all of the coefficients a^* and b^*. To have the fourth-order accuracy, we have to have a third-order polynomial profile at the cell faces. For a 2D problem, we assume the magnetic field at the cell faces has the following form:

$$B_x(x_i,y) = a^f_0(x_i) + a^f_2(x_i)y + \frac{1}{2}a^f_{22}(x_i)y^2 + \frac{1}{6}a^f_{222}(x_i)y^3, \tag{14}$$

$$B_y(x,y_j) = b^f_0(y_j) + b^f_1(y_j)x + \frac{1}{2}b^f_{11}(y_j)x^2 + \frac{1}{6}b^f_{111}(y_j)x^3, \tag{15}$$

where the superscript ^{f} denotes that the coefficient is for the face reconstruction. Eqs. (12) and (13) have a total of 20 coefficients. Enforcing the divergence-free condition of the magnetic field over the whole cell, we can obtain six constraints

$$a_1 + b_2 = 0; \quad a_{11} + b_{12} = 0; \quad a_{12} + b_{22} = 0;$$
$$a_{122} + b_{222} = 0; \quad a_{111} + b_{112} = 0; \quad a_{112} + b_{122} = 0.$$

Therefore we have only 14 independent coefficients in Eqs. (12) and (13). The third-order profile on the cell faces by Eqs. (14) and (15) has 16 defined coefficients, and only 15 of them are independent due to the divergence-free constraint. Hence the coefficients in Eqs. (12) and (13) are over-determined by the face profile. To resolve this issue, we add two more terms in both (12) and (13),

$$B_x(x,y) = a_0 + a_1 x + a_2 y + \frac{1}{2}a_{11}x^2 + a_{12}xy + \frac{1}{2}a_{22}y^2 + \frac{1}{6}a_{111}x^3 + \frac{1}{2}a_{112}x^2 y + \frac{1}{2}a_{122}xy^2 + \frac{1}{6}a_{222}y^3 + \frac{1}{24}a_{1111}x^4 + \frac{1}{6}a_{1222}xy^3, \tag{16}$$

$$B_y(x,y) = b_0 + b_1 x + b_2 y + \frac{1}{2}b_{11}x^2 + b_{12}xy + \frac{1}{2}b_{22}y^2 + \frac{1}{6}b_{111}x^3 + \frac{1}{2}b_{112}x^2 y + \frac{1}{2}b_{122}xy^2 + \frac{1}{6}b_{222}y^3 + \frac{1}{6}b_{1112}x^3 y + \frac{1}{24}b_{2222}y^4, \tag{17}$$

where we have a total of 24 coefficients. Imposing the divergence-free conditions in a continuous sense yields two additional constraints on the coefficients:

$$a_{1111} + b_{1112} = 0, \quad a_{1222} + b_{2222} = 0. \tag{18}$$

Thus we have total 16 independent coefficients in the polynomials given by (16) and (17). However, we have only 15 independently-defined coefficients by the face profiles. It seems that the information of reconstruction at four faces is not enough to construct a divergence-free fourth-order reconstruction over the whole cell. The problem lies in the mixed derivative a_{112} or b_{122}, which cannot be well-defined to achieve the fourth-order accuracy by just using the four-face profiles. One more constraint on the coefficients is needed to obtain a solvable system.

The extra constraint that uses the most compact stencil is from the V-cell,

$$\bar{b}^V_{x,i+\frac{1}{2}j} - \bar{b}^V_{x,i+\frac{1}{2}j-1} = \frac{1}{\Delta y}\left(\int_{y_{j+\frac{1}{2}}}^{y_{j+\frac{3}{2}}} B_1\left(x_{i+\frac{1}{2}}, y\right)dy - \int_{y_{j-\frac{1}{2}}}^{y_{j+\frac{1}{2}}} B_1\left(x_{i+\frac{1}{2}}, y\right)dy\right) = \left(a_2 + \frac{1}{12}a_{222}\Delta^2 y\right)\Delta y \tag{19}$$

Matching Eqs. (16) and (17) at the cell faces with Eqs. (14) and (15), and using the constraint (19) gives the following solutions for the coefficients

$$a_{12} = -b_{22} = \frac{a_2^{f_R} - a_2^{f_L}}{\Delta x}, \tag{20}$$

$$a_{22} = \frac{a_{22}^{f_L} + a_{22}^{f_R}}{2}, \tag{21}$$

$$a_{122} = -b_{222} = \frac{a_{22}^{f_R} - a_{22}^{f_L}}{\Delta x}, \tag{22}$$

$$a_{222} = \frac{1}{2}\left(a_{222}^{f_R} + a_{222}^{f_L}\right), \tag{23}$$

$$a_{1222} = -b_{2222} = \frac{a_{222}^{f_R} - a_{222}^{f_L}}{\Delta x}, \tag{24}$$

$$a_2 = \frac{\bar{b}^V_{x,i+\frac{1}{2}j} - \bar{b}^V_{x,i+\frac{1}{2}j-1}}{\Delta y} - \frac{1}{12}a_{222}\Delta^2 y, \tag{25}$$

$$a_{112} = -b_{122} = \left(\frac{1}{2}\left(a_2^{f_R} + a_2^{f_L}\right) - a_2\right)\frac{8}{\Delta^2 x}, \tag{26}$$

$$b_{12} = -a_{11} = \frac{b_1^{f_T} - b_1^{f_B}}{\Delta y}, \tag{27}$$

$$b_{11} = \frac{b_{11}^{f_B} + b_{11}^{f_T}}{2}, \tag{28}$$

$$b_{112} = -a_{111} = \frac{b_{11}^{f_T} - b_{11}^{f_B}}{\Delta y}, \tag{29}$$

$$b_{111} = \frac{1}{2}\left(b_{111}^{f_T} + b_{111}^{f_B}\right), \tag{30}$$

$$b_{1112} = -a_{1111} = \frac{b_{111}^{f_T} - b_{111}^{f_B}}{\Delta y}, \tag{31}$$

$$a_0 = \frac{1}{2}\left(a_0^{f_L} + a_0^{f_R}\right) - \frac{1}{8}a_{11}(\Delta x)^2 - \frac{1}{384}a_{1111}(\Delta x)^4, \tag{32}$$

$$b_0 = \frac{1}{2}\left(b_0^{f_B} + b_0^{f_T}\right) - \frac{1}{8}b_{22}(\Delta y)^2 - \frac{1}{384}b_{2222}(\Delta y)^4, \tag{33}$$

$$a_1 = \frac{a_0^{f_R} - a_0^{f_L}}{\Delta x} - \frac{1}{24}a_{111}(\Delta x)^2, \tag{34}$$

$$b_2 = \frac{b_0^{f_T} - b_0^{f_B}}{\Delta y} - \frac{1}{24}b_{222}(\Delta y)^2, \tag{35}$$

where the subscripts L, R, T, B denote the values at the left, right, top, and bottom faces, respectively for a specific cell.

Although the constraint (19) has fourth-order accuracy, the 2D reconstruction via (25) and (26) does not reduce to the 1D reconstruction for planar, grid-aligned flows. For example, for flow along the y-direction, the x-directives should be zero but a_{112} calculated using (26) may not be zero. After careful search among all the compact stencils without using additional ghost cells, we find the following fourth-order approximation from the overlapping cells

$$a_{112} = \frac{\left(\bar{b}^V_{x,i-\frac{1}{2},j} - 2\bar{b}^V_{x,i+\frac{1}{2},j} + \bar{b}^V_{x,i+\frac{3}{2},j}\right) - \left(\bar{b}^V_{x,i-\frac{1}{2},j-1} - 2\bar{b}^V_{x,i+\frac{1}{2},j-1} + \bar{b}^V_{x,i+\frac{3}{2},j-1}\right)}{(\Delta x)^2 \Delta y} \tag{36}$$

together with

$$a_2 = \frac{1}{2}\left(a_2^{f_R} + a_2^{f_L}\right) - \frac{1}{8}a_{112}\Delta^2 x. \tag{37}$$

It can be easily verified that $a_{112} = 0$ for flows along the y-direction.

For non-overlapping grid, the derivative a_{112} can be calculated as

$$a_{112} = \frac{a_{11,i+\frac{1}{2},j+1} - a_{11,i+\frac{1}{2},j-1}}{2\Delta y}, \tag{38}$$

where $a_{xx,}^{*}$ is calculated before hand using (27). This approach can be used in our method too but requires more ghost cells than either (19) or (36).

We remark that the higher-order terms in a_0 and b_0 are necessary in order to preserve the divergence-free condition during time integration.

Balsara [13] used an energy minimization procedure to determine coefficients a_{112} without the additional constraint (19) or (36). For a 2D problem, it leads to $a_{112} = 0$, which may not be a fourth-order accurate approximation to the derivatives a_{112} for a general problem.

3.5. Cubic reconstruction at the face for the magnetic field

In this subsection, we propose three approaches to construct a cubic polynomial for the face-centered magnetic field. We will take B_x^U at the face $x = x_i$ of the cell $C_{i+1/2,j+1/2}$ as an example.

3.5.1. Cubic reconstruction at the face using only a single grid information

The cubic reconstruction for the magnetic field at $x = x_i$ has form

$$b_x\left(x_i, y_{j+\frac{1}{2}}\right) = a_0^f\left(x_i, y_{j+\frac{1}{2}}\right) + a_2^f\left(x_i, y_{j+\frac{1}{2}}\right)y + \frac{1}{2}a_{22}^f\left(x_i, y_{j+\frac{1}{2}}\right)y^2 + \frac{1}{6}a_{222}^f\left(x_i, y_{j+\frac{1}{2}}\right)y^3. \tag{39}$$

For simplicity, we drop the coordinate x_i from Eq. (39) and integrate it over the three faces of U-cells: $\bar{b}_x^U(y_{i-1/2})$ of the cell $C_{i+1/2,j-1/2}$, $\bar{b}_x^U(y_{j+1/2})$ of the cell $C_{i+1/2,j+3/2}$, and $\bar{b}_x^U(y_{j+3/2})$ of the cell $C_{i+1/2,j+1/2}$, we have

$$\bar{b}_x^U\left(y_{i+\frac{1}{2}}\right) = a_0^f\left(y_{j+\frac{1}{2}}\right) + \frac{1}{24}a_{22}^f\left(y_{j+\frac{1}{2}}\right)(\Delta y)^2, \tag{40}$$

$$\bar{b}_x^U\left(y_{j-\frac{1}{2}}\right) = a_0^f\left(y_{j+\frac{1}{2}}\right) - a_2^f\left(y_{j+\frac{1}{2}}\right)\Delta y + \frac{13}{24}a_{22}^f\left(y_{j+\frac{1}{2}}\right)(\Delta y)^2 - \frac{5}{24}a_{222}^f(\Delta y)^3, \tag{41}$$

$$\bar{b}_x^U\left(y_{j+\frac{3}{2}}\right) = a_0^f\left(y_{j+\frac{1}{2}}\right) + a_2^f\left(y_{j+\frac{1}{2}}\right)\Delta y + \frac{13}{24}a_{22}^f\left(y_{j+\frac{1}{2}}\right)(\Delta y)^2 + \frac{5}{24}a_{222}^f(\Delta y)^3. \tag{42}$$

Since we have four coefficients in Eq. (39), we need another constraint in addition to Eqs. (40)–(42). We choose to use

$$\bar{b}_x^U\left(y_{i+\frac{5}{2}}\right) - \bar{b}_x^U\left(y_{i-\frac{5}{2}}\right) = 4a_2^f\left(y_{j+\frac{1}{2}}\right) + \frac{17}{6}a_{222}^f\left(y_{j+\frac{1}{2}}\right). \tag{43}$$

Solving the above equations, we obtain

$$a^f_{222}\left(y_{j+\frac{1}{2}}\right) = \frac{\bar{b}^U_x\left(y_{i+\frac{5}{2}}\right) - 2\bar{b}^U_x\left(y_{i+\frac{3}{2}}\right) + 2\bar{b}^U_x\left(y_{i-\frac{3}{2}}\right) - \bar{b}^U_x\left(y_{i-\frac{5}{2}}\right)}{2\Delta^3 y} \tag{44}$$

$$a^f_2\left(y_{j+\frac{1}{2}}\right) = \frac{\bar{b}^U_x\left(y_{j+\frac{3}{2}}\right) - \bar{b}^U_x\left(y_{j-\frac{1}{2}}\right)}{\Delta y} - \frac{5}{24}a^f_{222}\Delta^2 x, \tag{45}$$

$$a^f_{22}\left(y_{j+\frac{1}{2}}\right) = \frac{\bar{b}^U_x\left(y_{j+\frac{3}{2}}\right) - 2\bar{b}^U_x\left(y_{i+\frac{1}{2}}\right) + \bar{b}^U_x\left(y_{j-\frac{1}{2}}\right)}{(\Delta y)^2}, \tag{46}$$

$$a^f_0\left(y_{j+\frac{1}{2}}\right) = \bar{b}^U_x\left(y_{i+\frac{1}{2}}\right) - \frac{1}{24}a^f_{22}\left(y_{j+\frac{1}{2}}\right)(\Delta y)^2. \tag{47}$$

3.5.2. Cubic reconstruction at the face using the combined cells

The overlapping cells provide information to construct a more compact cubic polynomial. Similar to the third-order method [1], we construct a cubic divergence-free polynomial over a virtual cell that fully contains one cell boundary.

Take B^U_x at face $x = x_i$ of the cell $C_{i+1/2,j+1/2}$ as an example (see the left plot of Fig. 4). We choose the virtual cell to be $[x_{i-1/2}, x_{i+1/2}] \times [y_j, y_{j+1}]$. We assume the polynomials of B_x and B_y over the virtual cell have the same form as Eqs. (12) and (13), but the coefficients are estimated at the center $(x_i, y_{j+1/2})$ of the virtual cell.

As illustrated in Fig. 4, we will use the combined face-centered U-cell values and V-cell values to construct the third-order polynomial for B_x. The most difficult part is to find a^f_{222}. It requires at least four faces values in y-direction. We choose to use the four sums from the V-cells to achieve the fourth-order accuracy:

$$\begin{aligned}
b^{vTT}_x &= \bar{b}^V_x(x_{i-1/2}, y_{j+1}) + \bar{b}^V_x(x_{i+1/2}, y_{j+1}),\\
b^{vT}_x &= \bar{b}^V_x(x_{i-1/2}, y_j) + \bar{b}^V_x(x_{i+1/2}, y_j),\\
b^{vB}_x &= \bar{b}^V_x(x_{i-1/2}, y_{j-1}) + \bar{b}^V_x(x_{i+1/2}, y_{j-1}),\\
b^{vBB}_x &= \bar{b}^V_x(x_{i-1/2}, y_{j-2}) + \bar{b}^V_x(x_{i+1/2}, y_{j-2}),\\
a^f_{222}(x_i, y_{i+1/2}) &= \frac{b^{vTT}_x - 3b^{vT}_x + 3b^{vB}_x - b^{vBB}_x}{2\Delta^3 y}.
\end{aligned} \tag{48}$$

The other derivatives can be constructed using Eqs. (45)–(47).

The above reconstruction requires at least two ghost cells. To make it more compact, we use combined cells to construct a^f_{222} as follows:

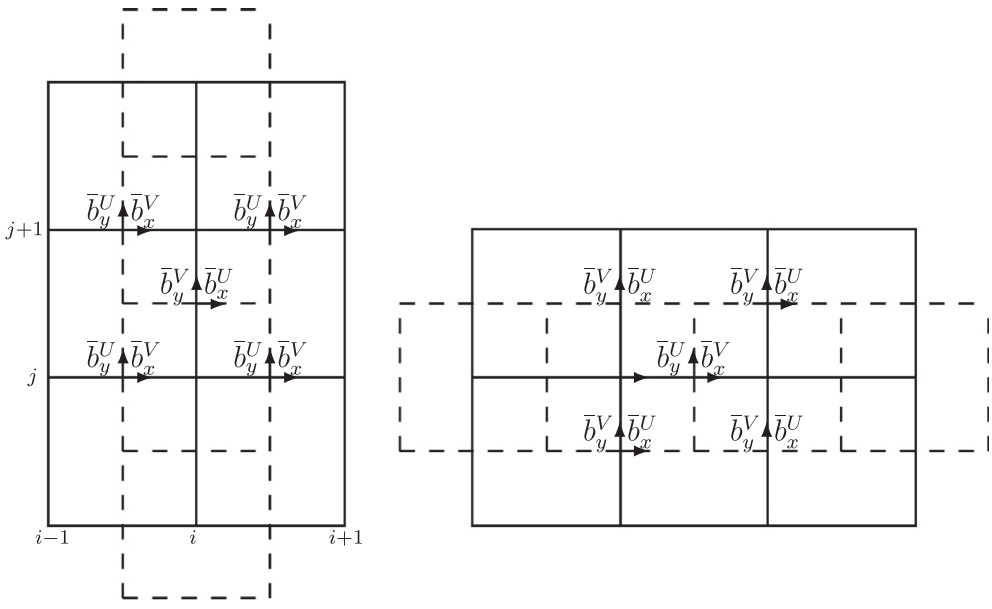

Fig. 4. The stencils used in parabolic reconstruction with the combined cell for the face-averaged magnetic fields. The dashed lines denote the boundaries of the V-cell, and the solid lines denote the boundaries of the U-cell. The left stencil is for the reconstruction of $\bar{b}^U_x$, and the right stencil is for the reconstruction of $\bar{b}^U_y$.

$$
\begin{aligned}
b_x^{uT} &= \left(\bar{b}_x^U(x_{i-1}, y_{j+1/2}\right) + \bar{b}_x^U(x_{i+1}, y_{j+1/2}) + 6\bar{b}_x^U(x_i, y_{j+1/2}),\\
b_x^{vT} &= 8\left(\bar{b}_x^V(x_{i-1/2}, y_j) + \bar{b}_x^V(x_{i+1/2}, y_j)\right),\\
b_x^{vB} &= 8\left(\bar{b}_x^V(x_{i-1/2}, y_{j-1}) + \bar{b}_x^V(x_{i+1/2}, y_{j-1})\right),\\
b_x^{uB} &= (\bar{b}_x^U(x_{i-1}, y_{j-3/2}) + \bar{b}_x^U(x_{i+1}, y_{j-3/2}) + 6\bar{b}_x^U(x_i, y_{j-3/2}),\\
a_{222}^f(x_i, y_{i+1/2}) &= \frac{\left(b_x^{uT} - b_x^{uB}\right) - \left(b_x^{vT} - b_x^{vB}\right)}{2\Delta^3 y}.
\end{aligned}
\tag{49}
$$

Eq. (49) has the same accuracy as (48), but requires only one ghost cell.

Both reconstructions (48) and (49) are more complicated than (44). However, by using the overlapping cells, the reconstructions become more compact. This can be seen from the radius of the disk that covers the reconstruction stencil. The radius is $2.5\Delta y$ for (44), $\sqrt{4\Delta^2 y + 0.25\Delta^2 x}$ for (48), and $\sqrt{2.25\Delta^2 y + \Delta^2 x}$ for (49) respectively. For a uniform grid with $\Delta x = \Delta y$, (49) is definitely more compact. We have verified that all of three reconstructions achieve the expected fourth-order accuracy and have found that (49) is the most accurate one with the smallest stencil. Therefore, (49) will be used in all of the numerical simulations presented in Section 5.

4. Non-oscillatory hierarchical central reconstruction using the second-degree remainder

The central reconstruction out of nearby cell averages generates a polynomial in each cell. For solutions that contain discontinuities, Gibbs phenomenon could appear in the reconstructed polynomials. Liu et al. [6] proposed a non-oscillatory hierarchical reconstruction (HR) procedure to remove the possible oscillations and achieve high resolution near discontinuities.

HR uses information from only the adjacent cells. It does not need local characteristic decomposition. However, small overshoots/undershoots after interactions of discontinuities can still be observed especially for fourth- and higher-order method. Liu et al.[7] proposed a new technique to lower the order of the remainder of the polynomial in the current cell during HR while maintaining the theoretical order of accuracy. Its application to the cell-centered variable in our MHD problem is straightforward.

Our fourth-order divergence-free reconstruction involves an additional constraint (19) or (36). The limited reconstruction for the face-centered magnetic field has little or no impact on the value of a_{112}. Since a_{112} does not affect the divergence-free condition, we obtain a limited a_{112} by applying HR to the cell-averaged magnetic fields. In the following, we will focus on the HR for the face-centered magnetic field.

4.1. Non-oscillatory hierarchical reconstruction using the second-degree remainder for the magnetic field

To preserve the divergence-free condition $\nabla\cdot\mathbf{B} = 0$, we must perform the non-oscillatory limiting processing to the central reconstruction of the magnetic field at the faces. Once we have a high order central reconstruction for the face-averaged magnetic field for every face, the divergence-free reconstruction described in Section 3.4 can be used as usual.

In [1] we described an HR method using only the single grid information. Here we describe an HR method using the combined U-cells and V-cells. Take the reconstruction of Eq. (14) and the U-face at $(x_i, y_{j+1/2})$ as an example. In the first step, we take the second derivative with respect to y in (14) and obtain

$$
L^U\left(y_{j+\frac{1}{2}}\right) = a_{22}^f\left(y_{j+\frac{1}{2}}\right) + a_{222}^f\left(y_{j+\frac{1}{2}}\right)y, \tag{50}
$$

where x_i is omitted from the equation for simplicity. For the faces $[y_{j+1/2}, y_{j+3/2}]$ and $[y_{j-1/2}, y_{j+1/2}]$, we take the second derivatives with respect to y in the reconstructed polynomial of V-cell at y_{j+1} and y_j,

$$
L^V(y_J) = a_{22}^V(y_J) + a_{222}^V(y_J)y, \quad J = j, j+1.
$$

Then we calculate the face average of L^U and L^V on their respective faces to obtain $\bar{L}^U(y_{j+1/2}) = a_{22}^f(y_{j+1/2})$ and $\bar{L}^V(y_J) = a_{22}^V(y_J)$, $J = j, j+1$. With the three new face averages, we can apply the center biased ENO limiter function to calculate a new $\tilde{a}_{222}^f$, which is

$$
\tilde{a}_{222}^f = \mathrm{ENO}_\epsilon\left(\frac{\bar{L}^U\left(y_{j+\frac{1}{2}}\right) - \bar{L}^V(y_j)}{0.5\Delta y}, \frac{\bar{L}^V(y_{j+1}) - \bar{L}^U\left(y_{j+\frac{1}{2}}\right)}{0.5\Delta y}\right). \tag{51}
$$

where the ENO limiter is defined as

$$
\mathrm{ENO}(c_1, c_2, \ldots, c_m) = c_j, \quad \text{if } |c_j| = \min(|c_1|, |c_2|, \ldots, |c_m|). \tag{52}
$$

and the center biased ENO limiter is defined as

$$\mathrm{ENO}_\epsilon(c_1,c_2,\ldots,c_m)=\mathrm{ENO}\left((1+\epsilon)\mathrm{ENO}(c_1,c_2,\ldots,c_m),\frac{1}{m}\sum_{i=1}^{m}c_i\right). \tag{53}$$

The ENO procedure can be replaced with an MUSCL procedure by a different limiter, such as minmod limiter, van Leer limiter, Woodward limiter, and super-bee limiter.

In the second step, we calculate the first derivative with respect to y in Eq. (14) and obtain its linear part by

$$L^U\left(y_{j+\frac{1}{2}}\right)=a_2^f\left(y_{j+\frac{1}{2}}\right)+a_{22}^f\left(y_{j+\frac{1}{2}}\right)y+\frac{1}{2}\left(a_{222}^f\left(y_{j+\frac{1}{2}}\right)-\tilde{a}_{222}^f\left(y_{j+\frac{1}{2}}\right)\right)y^2. \tag{54}$$

Similarly, we take the first derivative with respect to y in the reconstructed polynomial of V-cell at $y=y_J, J=j, j+1$, and obtain their linear parts

$$L^V(y_J)=a_2^V(y_J)+a_{22}^V(y_J)y+\frac{1}{2}\left(a_{222}^V(y_J)y^2-\tilde{a}_{222}^f\left(y-y_{j+\frac{1}{2}}\right)^2\right),\quad J=j,j+1.$$

Note that $\tilde{a}_{222}$ is the newly updated derivative from the first step. Calculating the face-averaged values of L^U and L^V at their respective faces, and applying again the center biased ENO limiter (51), we obtain a new limited second-order derivative $\tilde{a}_{22}^f$.

In the third step, we will use the second-degree remainder technique [7] to calculate $\tilde{a}_y^f$. Rewriting the cubic polynomials of V-cell at $(i,J), J=j, j+1$ with the origin at $\left(x_i,y_{j+\frac{1}{2}}\right)$, we obtain the linear parts of the three cubic polynomials as

$$L^U\left(y_{j+\frac{1}{2}}\right)=a_0\left(y_{j+\frac{1}{2}}\right)+a_2^f\left(y_{j+\frac{1}{2}}\right)y+\frac{1}{2}\left(a_{22}^f-\tilde{a}_{22}^f\right)\left(y_{j+\frac{1}{2}}\right)y^2, \tag{55}$$

$$L^V(y_J)=a_0^{V_J}\left(y_{j+\frac{1}{2}}\right)+a_2^{V_J}\left(y_{j+\frac{1}{2}}\right)y+\frac{1}{2}\left(a_{22}^{V_J}-\tilde{a}_{22}^f\right)\left(y_{j+\frac{1}{2}}\right)y^2,\quad J=j,j+1, \tag{56}$$

where the new coefficients $a_{(*)}^{V_J}$ are derived from the reconstructed polynomial of V-cell V_J by moving the origin to $\left(x_i,y_{j+\frac{1}{2}}\right)$. Calculating the face-averaged values of L^U and L^V again at their respective faces, we obtain a new limited first-order derivative $\tilde{a}_y^f$.

To preserve the face-averaged value, we set

$$\tilde{a}_0^f=\bar{b}_{x,i,j+\frac{1}{2}}-\frac{1}{24}\tilde{a}_{22}^f(\Delta y)^2. \tag{57}$$

Finally, we obtain the cubic non-oscillatory reconstruction

$$\tilde{b}_x\left(x_i,y_{j+\frac{1}{2}}\right)=\tilde{a}_0^f+\tilde{a}_2^f\left(y-y_{j+\frac{1}{2}}\right)+\frac{1}{2}\tilde{a}_{22}^f\left(y-y_{j+\frac{1}{2}}\right)^2+\frac{1}{6}\tilde{a}_{222}^f\left(y-y_{j+\frac{1}{2}}\right)^3. \tag{58}$$

5. Numerical experiment

In this section, we provide some examples to test our fourth-order schemes with divergence-free reconstruction. To achieve the fourth-order in time, we apply the fourth-order five-stage strong stability preserving Runge–Kutta (SSP-RK) time integration [14]. For comparison, we also test our code with classical fourth-order four-stage RK method.

As pointed out in [6], the HR is expensive and takes about 64% of CPU time for our fourth-order scheme. As in [6], we use a low cost smoothness detector which measures the jump of the solution at the cell-center from reconstruction of neighbor cells. If the jump is smaller than $(\Delta x)^2$, the cell is considered to be in the smooth region and the hierarchical reconstruction procedure will not be performed. Usually the density and pressure are chosen as the candidate variables in the smoothness detector.

For comparison, we quantify the divergence of the magnetic field at the cell center using

$$\nabla\cdot\mathbf{B}=a_1+b_2, \tag{59}$$

where a_1 and b_2 are the coefficients of the first-order terms in the reconstructed polynomial of B_x and B_y, respectively.

The time step is determined by the CFL condition, which depends on the cell size and maximum signal speed over the whole domain. Without specification, the CFL number of 0.48 is used. Unless specified otherwise, we will use $\gamma=5/3$. For all the examples, we show only the numerical results of the U-cells.

5.1. Circularly polarized Alfvén wave

We first solve the smooth Alfvén wave problem [11] to verify the accuracy of our proposed scheme. This problem describes propagation of a circularly polarized Alfvén wave in the domain $[0,1/\cos\alpha]\times[0,1/\sin\alpha]$ where α is the wave propagation angle relative to the x-axis. The initial conditions are taken as

$$\rho=1,\quad v_\parallel=0,\quad v_\perp=0.1\sin(2\pi\xi),\quad v_z=0.1\cos(2\pi\xi),$$
$$p=0.1,\quad B_\parallel=1,\quad B_\perp=v_\perp,\quad B_z=v_z,$$

where $\xi = x\cos(\alpha) + y\sin(\alpha)$. In this problem, the Alfvén wave propagates periodically towards the origin with a constant Alfvén speed $B_\parallel/\sqrt{\rho} = 1$ and returns to its initial state whenever t becomes an integer. In our test, we use $\alpha = 45°$. The domain is divided into $N \times N$ grid. As in [11], for each N, we estimate the relative numerical error of any fluid variable v by

$$\delta_N(v) = \frac{\sum_{j=1}^{N}\sum_{k=1}^{N}|v_{j,k}^{N} - v_{j,k}^{\text{exact}}|}{\sum_{j=1}^{N}\sum_{k=1}^{N}|v_{j,k}^{\text{exact}}|}. \tag{60}$$

Table 1 shows that average numerical errors defined by

$$\delta_N = \frac{1}{4}(\delta_N(v_\perp) + \delta_N(v_z) + \delta_N(B_\perp) + \delta_N(B_z)),$$

and the corresponding convergence orders, defined by $R_N = \log(\delta_N/\delta_{N/2})/\log(2)$, for both divergence-free constrained transport (CT) method, which is described in Section 3.3), and non-CT central schemes when the limiting via HR is not used. The results show clearly that we have achieved the expected fourth-order accuracy for both CT and non-CT methods. For comparison, we also show the numerical errors of the third-order schemes [1]. The computational cost of the fourth-order method is only double the cost of the third-order method for a grid of 64×64. However the accuracy of the fourth-order method on a grid of 64×64 is corresponding to that of 256×256 grid of the third-order method. Therefore to achieve the same accuracy, the fourth-order method is about 32 times more efficient than the third-order method.

Table 2 shows the numerical errors and convergence order when the limiting via HR is used. Since this is a smooth problem, the discontinuity detector will not activate the limiting procedure. We turn off the detector for this specific test so that limiting is used everywhere during reconstruction step. Table 2 shows that we still achieve approximately fourth-order accuracy with limiting.

5.2. Vortex propagation problem

This test problem was proposed by Balsara [15] for accuracy analysis. The problem is defined in a periodic domain $[-5,5] \times [-5,5]$ with mean flow $(\rho, P, v_x, v_y, B_x, B_y) = (1,1,1,1,0,0)$. The perturbed velocity and magnetic fields are given by

$$(\delta v_x, \delta v_y) = \frac{\kappa}{2\pi}e^{0.5(1-r^2)}(-y,x),$$
$$(\delta B_x, \delta B_y) = \frac{\mu}{2\pi}e^{0.5(1-r^2)}(-y,x).$$

The vortex propagates along the diagonal direction with period of 10. The pressure determined by the dynamical balance is given by

$$\delta P = \frac{\kappa^2(1-r^2) - \mu^2}{8\pi^2}e^{1-r^2},$$

where the scaling factor $1/\sqrt{4\pi}$ in the original set-up of [15] has been incorporated into the MHD equations and is not shown here.

Table 1
Numerical errors (δ_N) and convergence order (R_N) for the smooth Alfvén wave problem at $t = 2$ with and without CT. The limiter is not used.

N	Non-CT 3rd		Non-CT 4th		CT 3rd		CT 4th	
	δ_N	R_N	δ_N	R_N	δ_N	R_N	δ_N	R_N
16	0.0663255	–	0.0038659	–	0.0709366	–	0.0040095	–
32	0.0085469	2.96	0.0002169	4.15	0.0092040	2.95	0.0002308	4.12
64	0.0010724	2.99	1.310E−05	4.05	0.0011562	2.99	1.407E−05	4.04
128	0.0001341	3.00	8.129E−07	4.01	0.0001446	3.00	8.750E−07	4.01

Table 2
Numerical errors (δ_N) and convergence order (R_N) for the smooth Alfvén wave problem at $t = 2$ with and without CT when the limiting is used everywhere during the reconstruction.

N	Non-CT 4th		CT 4th	
	δ_N	R_N	δ_N	R_N
16	0.03368	–	0.02602	–
32	0.0003743	6.49	0.0003416	6.25
64	3.3472E−5	3.48	2.4451E−5	3.80
128	2.3556E−6	3.82	1.6995E−6	3.85
256	1.6057E−7	3.87	1.1419E−7	3.89
512	1.1306E−8	3.82	8.4139E−9	3.76

We solve the problem with $\kappa = \mu = 5$, which yields a stronger vortex than the original setting $\kappa = \mu = 1$ of [15]. The accuracy of the initial condition is crucial to the convergence test for this problem. Since our numerical method is based on the finite-volume formulation on the cell-averaged quantities, the initial conditions will have truncation errors if we initialize them as point values at the cell center. Such error will not affect the convergence order for the low-order (<4) method because the midpoint rule has the third-order accuracy. The complete set of cell-averaged initial conditions for this problem can be obtained easily by using analytical integral.

Another factor that affects the convergence order is the domain definition. If we use the above initial conditions on a periodic domain $[-5,5] \times [-5,5]$, then the error at the domain boundary is $O(e^{-12}) \approx O(10^{-6})$. Any numerical error lower than that will be contaminated. Due to this initial error at domain boundaries, we cannot obtain the expected convergence order when the grid is refined sufficiently.

We calculate the average errors of four variables v_x, v_y, b_x, b_y and the convergence orders after one period ($t = 10$). Table 3 shows the data without limiter for domain $[-5,5] \times [-5,5]$. Because no limiter is used for this test, the convergence rate should be close to fourth-order. However, Table 3 shows clearly that the convergence order drops to smaller than two with the more refined grids for both the cell-averaged (denoted as "CA" in the table) and the point-value (denoted as "PV" in the table) initial conditions (IC). The divergence error max $(\nabla \cdot \mathbf{B})$ keeps the level $O(10^{-6})$ no matter what refinement we use. We have verified that the maximum divergence error for the fine grids occurs at the domain boundary rather than at the center of the vortex. The large error at the domain boundary was also pointed out in Dumbser et al. [16].

To reduce the error related to the domain boundary, we extend our periodic domain to $[-10,10] \times [-10,10]$. The error with respect to the smoothness at the domain boundary becomes $O(e^{-49.5}) \approx O(10^{-22})$, which is below the double precision requirement.

Table 4 shows the errors for the extended domain. Since no limiter is used, the convergence rate should be fourth-order. The solution with cell-averaged (CA in the table) initial conditions (IC) converges as expected. However the convergence rate for the solutions with midpoint initial conditions decreases to the second-order for the refined grid.

We now study the impact of the limiters for this problem. Table 5 shows the errors and convergence rate at one period ($t = 20$) for the extended domain $[-10,10] \times [-10,10]$. It is clear that the only the divergence-free CT method with cell-averaged initial condition achieves the expected order of accuracy for both coarse and fine grids. Compared with the data in Table 4, the error for the CT method is double due to the limiter. Again, the convergence rate for the point-value initial condition is degenerated into second-order at fine grid.

Table 5 also shows that the error for the non-CT method is at least twice as large as that for the CT method. We have found that the drop of accuracy for the non-CT method in Table 5 is mainly due to the divergence error of the magnetic field. In fact, the convergence error increases dramatically after four periods ($t = 80$) for the extended domain. Fig. 5 shows the results of divergence error of the magnetic fields for grids with different resolutions. For both 200×200 and 400×400 grids, the maximum of $|\nabla \cdot \mathbf{B}|$ increases exponentially at some time and degenerates the accuracy of the numerical methods. Fig. 6 shows the comparison in the contour plots of pressure with and without divergence-free CT method.

Table 6 shows the error and convergence order at $t = 80$ for the extended domain. It is clear that solution without divergence-free CT method does not converge when the grid is refined from 200×200 to 400×400. This indicates that the divergence error of the magnetic field cannot be neglected for a long-time integration if the limiter is used.

Table 3
Numerical errors (δ_N) and convergence order (R_N) for the vortex problem at $t = 10$ without CT and limiters for periodic domain $[-5,5] \times [-5,5]$. CA denotes cell average and PV denotes point value.

N	Non-CT 4th CA IC			Non-CT 4th PV IC		
	δ_N	R_N	max$(\nabla \cdot \mathbf{B})$	δ_N	R_N	max $(\nabla \cdot \mathbf{B})$
50	9.99E−4	–	9.23E−5	9.77E−4	–	9.2344E−5
100	5.12E−5	4.28	5.46E−6	5.96E−5	4.03	5.8686E−6
200	4.85E−6	3.40	2.36E−6	1.09E−5	2.45	2.3545E−6
400	1.44E−6	1.75	2.10E−6	3.39E−6	1.68	2.1027E−6

Table 4
Numerical errors (δ_N) and convergence order (R_N) for the vortex problem at $t = 20$ with and without CT for extended periodic domain $[-10,10] \times [-10,10]$. Limiter is not used.

N	Non-CT CA IC			Non-CT PV IC			CT CA IC		CT PV IC	
	δ_N	R_N	$\lvert\nabla \cdot B\rvert$	δ_N	R_N	$\lvert\nabla \cdot B\rvert$	δ_N	R_N	δ_N	R_N
50	3.88E−2	–	9.99E−3	3.98E−2	–	1.04E−3	3.22E−2	–	3.24E−2	–
100	1.76E−3	4.42	1.01E−4	1.74E−3	4.51	1.02E−4	1.52E−3	4.40	1.70E−3	4.25
200	8.53E−5	4.29	5.52E−6	8.40E−5	4.37	5.79E−6	8.11E−5	4.22	1.41E−4	3.59
400	4.80E−6	4.13	3.45E−7	8.69E−6	3.27	4.64E−7	4.79E−6	4.08	2.67E−5	2.40
800	2.90E−7	4.03	2.14E−8	2.04E−6	2.09	3.50E−8	2.94E−7	4.02	6.42E−6	2.05

Table 5
Numerical errors (δ_N) and convergence order (R_N) for the vortex problem at $t = 20$ with and without CT for extended periodic domain $[-10,10] \times [-10,10]$, Limiter is used everywhere during the reconstruction.

N	Non-CT CA IC			Non-CT midpoint IC			CT CA IC		CT midpoint IC	
	δ_N	R_N	$\lvert\nabla \cdot B\rvert$	δ_N	R_N	$\lvert\nabla \cdot B\rvert$	δ_N	R_N	δ_N	R_N
50	2.00E−1	–	4.43E−2	2.03E−1	–	4.55E−2	9.66E−2	–	9.60E−2	–
100	2.05E−2	3.28	3.77E−2	2.08E−2	3.28	3.82E−2	5.84E−3	4.04	5.79E−3	4.05
200	8.93E−4	4.52	1.30E−2	1.22E−3	4.09	1.32E−3	1.64E−4	5.15	2.27E−4	4.67
400	2.73E−5	5.03	1.02E−5	1.33E−4	3.20	9.68E−6	1.07E−5	3.94	3.13E−5	2.85
800	1.86E−6	3.88	1.29E−6	3.15E−5	2.09	1.51E−6	6.56E−7	4.02	6.56E−6	2.25

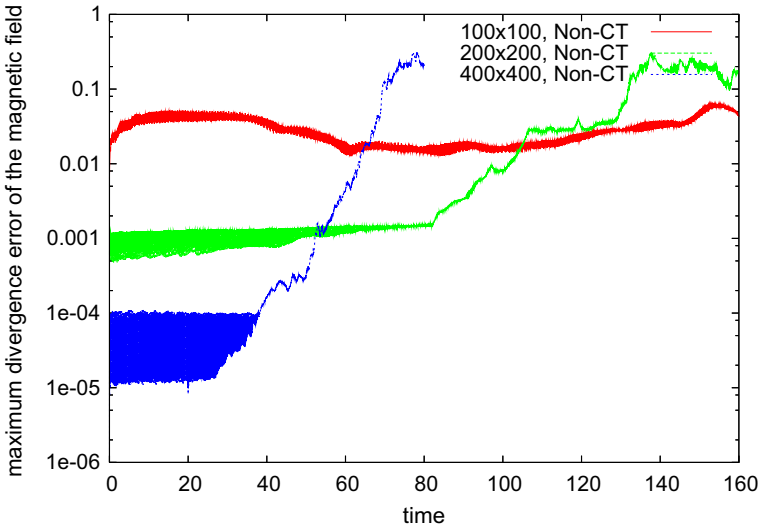

Fig. 5. Log–linear plot of the divergence error of the magnetic field.

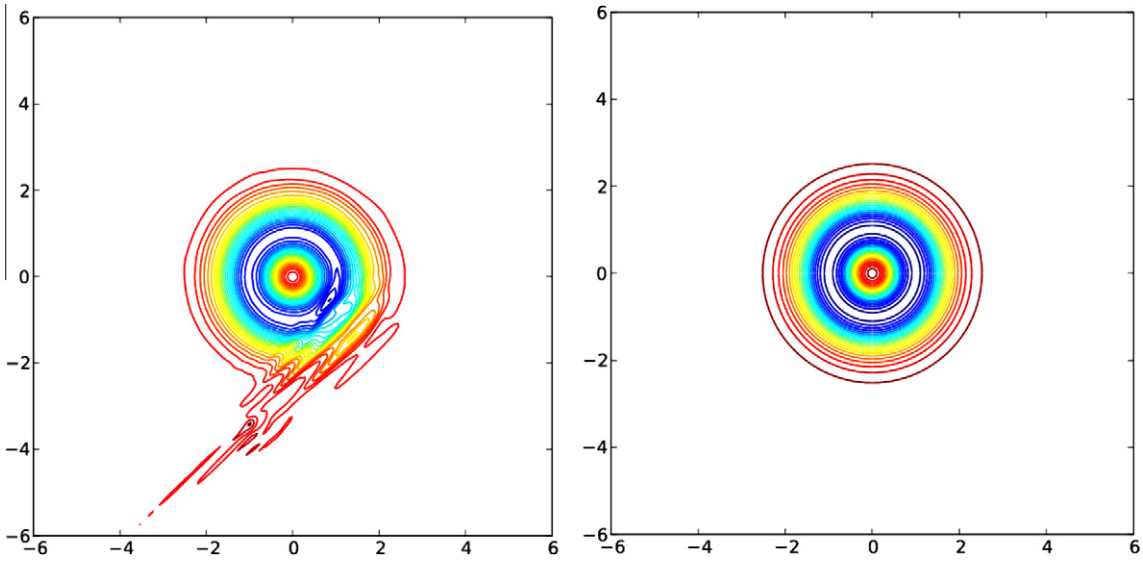

Fig. 6. Contour-plot for the pressure of the vortex problem at $t = 80$. The left is for the non-CT method, and the right is for the divergence-free CT method. Thirty contours are used.

Dumbser et al. [16] suggested another approach to reduce the error at the domain boundary without using the extended domain. They introduce a parameter q in the initial conditions,

Table 6
Numerical errors (δ_N) and convergence order (R_N) for the vortex problem at $t = 80$ for simulations with limiters. The periodic domain $[-10,10] \times [-10,10]$ and cell-averaged initial conditions are used.

N	Non-CT			CT	
	δ_N	R_N	$\max(\nabla \cdot \mathbf{B})$	δ_N	R_N
50	0.840	–	0.0331	0.218	–
100	0.193	2.12	0.0151	0.018	3.60
200	8.57E−3	4.49	0.0015	5.38E−4	5.06
400	8.64E−2	−3.33	0.2051	3.78E−5	3.83

$$(\delta v_x, \delta v_y) = \frac{\kappa}{2\pi} e^{q(1-r^2)}(-y, x), \tag{61}$$

$$(\delta B_x, \delta B_y) = \frac{\mu}{2\pi} e^{q(1-r^2)}(-y, x) \tag{62}$$

with a balanced pressure given by

$$\delta P = \frac{\kappa^2(1-2qr^2) - \mu^2}{16q\pi^2} e^{2q(1-r^2)}. \tag{63}$$

For $q = 1$, the error at the boundary becomes $O(e^{-24}) \approx O(10^{-11})$. Dumbser et al. [16] also pointed out that the correct convergence rates cannot be obtained without the use of divergence-cleaning approach proposed in [17]. For comparison, we solve the problem with initial conditions given by (61)–(63). We apply two approaches to reduce the divergence error when the limiter is applied everywhere. The first one is the eight-wave approach of Powell [18], and the other is the hyperbolic cleaning approach of [16]. For the first approach, the $\nabla \cdot \mathbf{B}$ related source term is only applied to the induction equation and therefore the momentum and energy is conserved. We remark that the full eight-wave approach of Powell [18] does not work well for this problem. For the second approach the artificial speed of the divergence error is $c_h = 1$. Fig. 7 shows the divergence error of the magnetic field for different approaches. It is interesting to see that the divergence error is smaller initially (before $t = 22$) for the approach without divergence cleaning than both divergence-cleaning approaches.

Fig. 7 shows that the hyperbolic cleaning is effective in controlling the divergence error of the magnetic field for a long-time integration. However, it is not favorable when compared with the divergence-free CT method. Table 7 shows comparison in numerical errors and convergence orders between the two approaches. The output is at five periods ($t = 50$). For a fair comparison, only the cell-averaged initial values are used.

5.3. Numerical dissipation and long term decay of Alfvén waves

Next we consider another problem proposed by Balsara [15], which tried to quantify the amount of numerical dissipation introduced by a numerical scheme for ideal MHD. Specifically, the test problem measures the decay of the amplitude of a

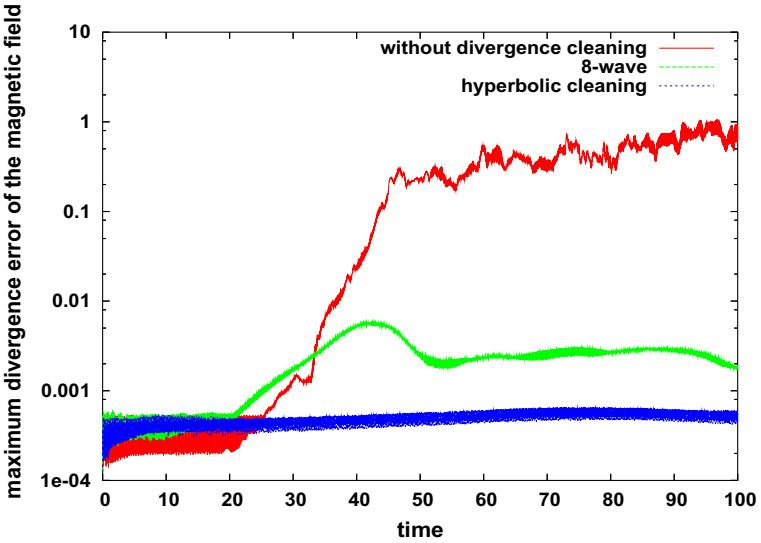

Fig. 7. Log–linear plot of the divergence error of the magnetic field for different approaches applied to the vortex problem. 200×200 grid is used. Limiter is used everywhere.

Table 7
Numerical errors (δ_N) and convergence order (R_N) for the vortex problem at $t = 50$ for simulations with limiters. The periodic domain $[-5,5] \times [-5,5]$ and cell-averaged initial conditions (61)–(63) are used. The divergence error for the CT method is $O(10^{-15})$.

N	Non-CT with hyperbolic cleaning			CT	
	δ_N	R_N	$\max(\nabla \cdot \mathbf{B})$	δ_N	R_N
50	0.300	–	4.35E−2	7.65E−2	–
100	3.53E−2	3.09	3.03E−2	2.16E−3	5.15
200	5.76E−4	5.94	5.45E−4	1.47E−4	3.87
400	5.74E−5	3.33	1.12E−4	9.78E−6	3.91

linearly degenerate Alfvén wave that propagates at a shallow angle to the y-axis. We use the same angle, $\alpha = \tan(1/6) = 9.462°$, and the same set of initial conditions as Balsara [15] except that the magnetic field is normalized with a $1/\sqrt{4\pi}$ factor. With the normalization, the B_z and v_z have the same exact solutions and thus have similar decay rates.

The computation domain is $[-3,3] \times [-3,3]$ on a 120×120 grid and the output time is $t = 129$. The maximum values of the v_z and B_z should remain constant in time for the exact solution, but decay due to the numerical dissipation. These quantities are plotted versus time in Fig. 8. Since B_z and v_z have similar decay rates, we plot here only the result of v_z. For comparison, we also provide the result of our third-order method. For the limited reconstruction results, we turn off the discontinuity detection so that the limiter is used everywhere.

Fig. 8 shows that our fourth-order method has much less numerical dissipation than the third-order method. It also shows that the divergence-free CT procedure is essential to achieve low-dissipation when the limiter is used. Otherwise, the divergence error of the magnetic field can grow exponentially at certain time ($t = 75$) and degenerate the accuracy of the solution. We remark that the divergence error does not increase much for the third-order method when the limiter is used, as shown in the bottom right plot of Fig. 8.

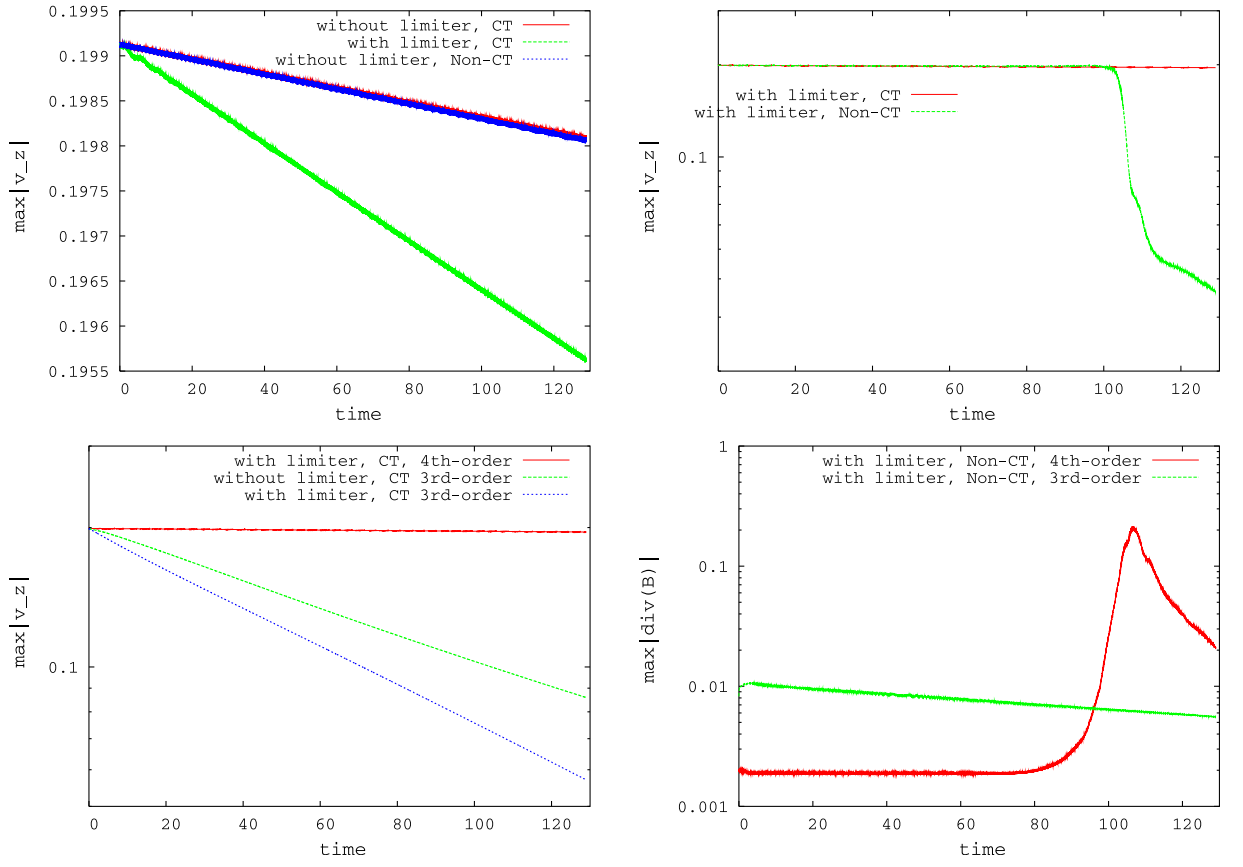

Fig. 8. Plots for the decay Alfvén waves. The *top left* plot shows linear–linear plot for the maximum value of z-component of the velocity (v_z). The results for the two methods without limiter almost overlays on each other. The *top right* plots shows the log-linear plot for v_z with limiters between CT and non-CT methods. The non-CT method has larger error than the divergence-free CT method. The *bottom left* plots shows the comparison between the fourth-order method and the third-order method. The *bottom right* plots shows the divergence errors for the non-CT fourth- and third-order method when the limiter is used. The divergence errors for all CT methods are of $O(10^{-14})$.

5.4. Orszag–Tang MHD turbulence problem

The problem is a compressible 2D vortex problem and contains many significant features of MHD turbulence. It has becomes a standard test problem for 2D numerical MHD simulations (e.g., [8,19,10]). The initial conditions are $v_x = -\sin(y)$, $v_y = \sin(x)$, $B_x = -\sin(y)$, $B_y = \sin(2x)$, $\rho = \gamma^2$, $p = \gamma$, $v_z = B_z = 0$. The computational domain is a square $[0,2\pi] \times [0,2\pi]$ with periodic boundary conditions along both boundaries. The final output time is $t = \pi$.

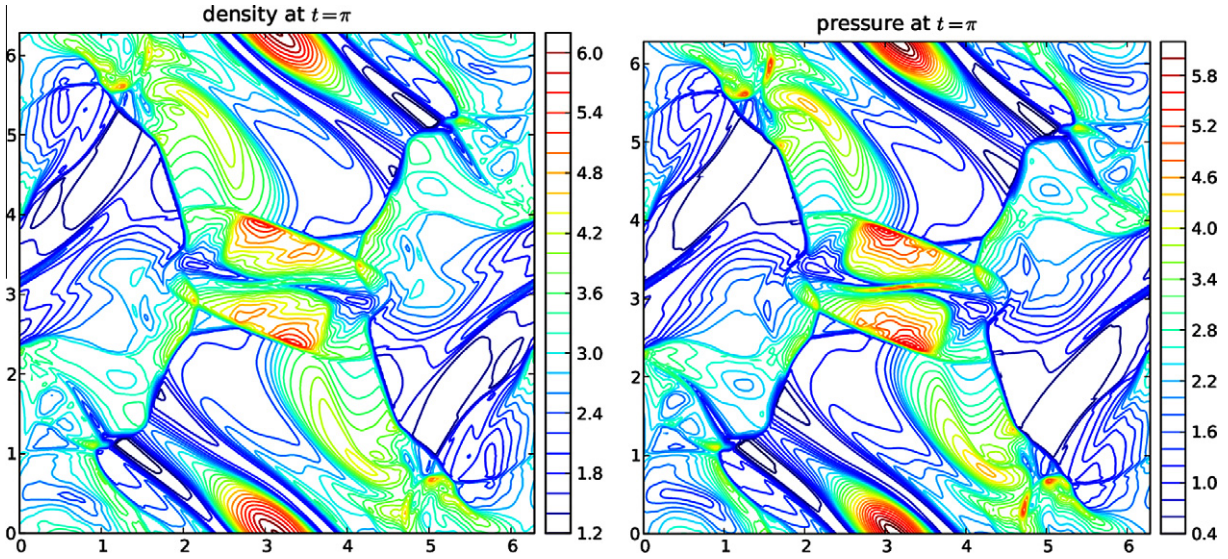

Fig. 9. The density and pressure contour plot at $t = \pi$ for the Orszag–Tang vortex problem. Thirty contours are used.

Table 8
Convergence of averaged relative errors in the Orszag–Tang vortex problem.

	$t = 0.633$				$t = 3.14$			
	$\bar{\delta}_{64}$	$\bar{\delta}_{128}$	$\bar{\delta}_{256}$	$\bar{\delta}_{512}$	$\bar{\delta}_{64}$	$\bar{\delta}_{128}$	$\bar{\delta}_{256}$	$\bar{\delta}_{512}$
CT	3.10E−4	2.67E−5	1.31E−6	5.27E−8	3.32E−2	1.95E−2	1.04E−2	4.36E−3
Non-CT	3.11E−4	1.77E−5	1.31E−5	5.24E−8	3.52E−2	2.92E−2	1.26E−2	6.57E−3

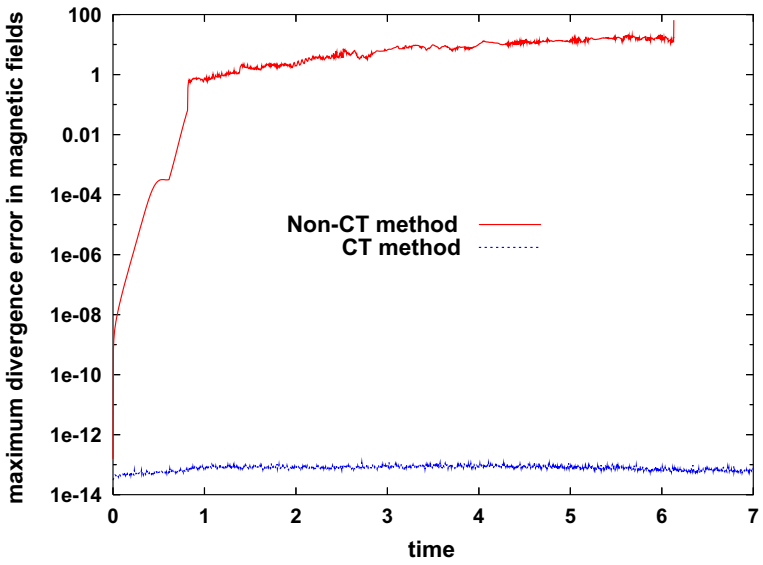

Fig. 10. The log–linear plot for the maximum divergence error of the magnetic field versus time at $t = \pi$ for the Orszag–Tang vortex problem.

Fig. 9 shows contour plots for the density and pressure at time $t = \pi$ on a 256×256 grid. Our results compare well with those given in [8,11].

The Orszag–Tang vortex problem starts from smooth initial condition data, but gradually the flow becomes very complex towards turbulence. Table 8 lists the average relative errors for the primitive variables for four resolutions (64×64, 128×128, and 256×256, 512×512). The reference solution is calculated with 1024×1024 grid. At time $T = 0.633$, the flow is still quite smooth, although some discontinuities are already present. We achieve fourth-order accuracy for both the CT scheme and non-CT schemes at $T = 0.633$. However, the solutions converge with only first-order accuracy at $T = \pi$, when the shock is dominant in the problem.

Table 8 shows that the non-CT method is comparable to the divergence-free CT method at both output times. However, when we continue the time integration, we found the divergence error for the non-CT method will grow rapidly with the time evolution and eventually break down the simulation due to the negative pressure and density in the solutions. For 256×256 grid, the negative pressure occurs at about $t = 4.34$ and negative density occurs at about $t = 6.13$. Fig. 10 shows the evolution of the divergence error for both CT and non-CT method. The error for the non-CT method grows up to 70 at $t = 6.13$.

The divergence-free scheme is essential for the high-order method to avoid the local instability due to the divergence error (see [19]). Even the local divergence-free method is not sufficient (see [20]) for this problem if the high-order elements (e.g., P_2 elements are used in a discontinuous Galerkin method in [20]) are used. Surprisingly, our third-order method does not have such kind of problems. The divergence error for the third-order non-CT method, which is not shown here, begins to

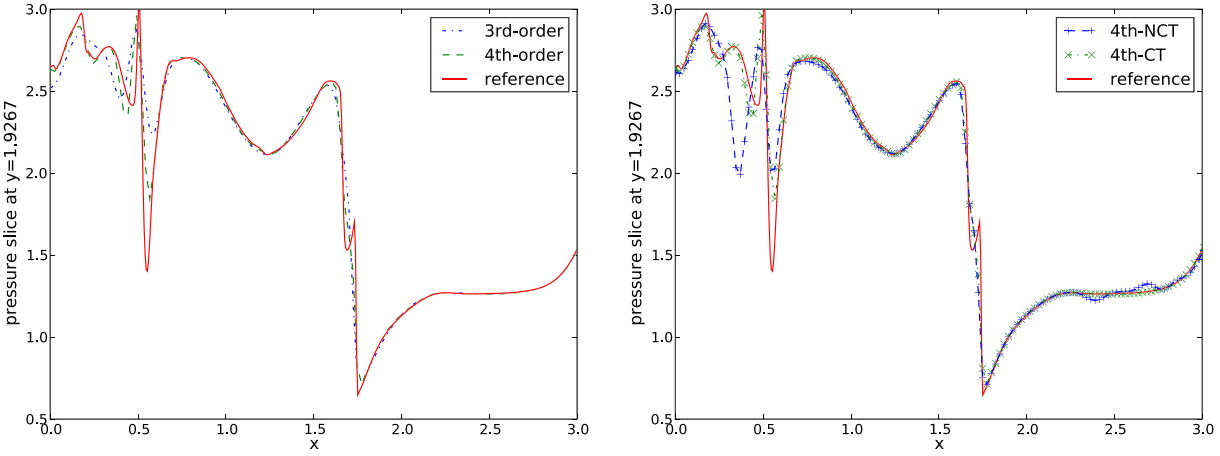

Fig. 11. The pressure slices at $t = \pi$ and $y = 1.9267$ for the Orszag–Tang vortex problem.

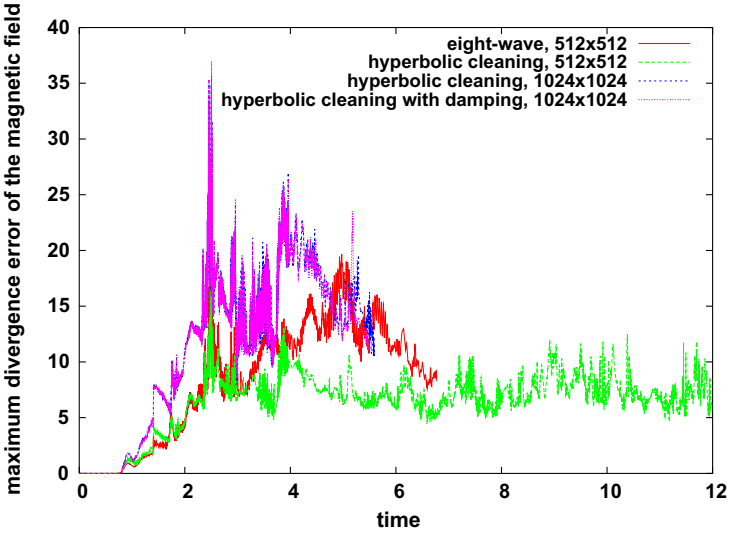

Fig. 12. The linear–linear plot for the maximum divergence error of the magnetic field versus time for the Orszag–Tang vortex problem. Without divergence-free method, all simulations presented here exit before reaching the final output time $t = 60$.

decay after it reaches some maximum value (≈ 6) at about $t = 4.11$. Fig. 11 shows the difference between the third-order method and the fourth-order method, and difference between with and without CT procedure. Clearly the fourth-order CT method is closer to the reference solution, which is calculated using the third-order CT method with 1024×1024 grid. It also shows that the shock front is resolved very well without oscillations. The right plot of Fig. 11 shows that non-CT method introduces some oscillations to the smooth region near $x = 2.5$. We found that these oscillations are purely effects of the divergence error introduced near the discontinuities. This indicates the importance of the divergence-free procedure in the wave development into small scales.

We have also tested the two divergence-cleaning approaches described in Section 5.2. The simulation with modified eight-wave approach runs smoothly without negative pressure and density for 256×256 grid, but failed at $t = 6.78$ for 512×512 grid due to the negative pressure. The simulation with hyperbolic cleaning approach runs well for both 256×256 and 512×512 grids but failed at $t = 5.59$ for 1024×1024 grid due to the negative pressure. Including parabolic damping factor $c_r = 0.18$ in the hyperbolic cleaning as suggested in [17] does not help much. The divergence errors for these approaches are shown in Fig. 12.

6. Conclusion

We have extended our third-order divergence-free method to the fourth-order. Numerical examples show that we have truly achieved the expected order accuracy for smooth problems with and without limited reconstruction.

Several examples show that the divergence-free CT method is essential for our fourth-order method to achieve the high-order accuracy. Without CT, the divergence error can grow rapidly and introduce instability to the solutions. This is quite different from what we obtain for the third-order method [1]. This instability may not show up for just a short-time integration, as shown in our examples for both smooth and discontinuous problems. But our divergence-free procedure is definitely needed for the stability in a long-time integration.

Our fourth-order method also shows very low-dissipation compared with the third-order method. The extension of our methods to 3D problem is currently in progress and will be reported elsewhere. The high-order, low-dissipation, and divergence-free properties of this method make it an ideal tool for direct MHD turbulence simulations.

Acknowledgements

The authors thank Dr. Yingjie Liu of Gatech for many useful discussions. We also thank referees for many useful comments. This research was performed under the auspices of the Department of Energy. It was supported by the Laboratory Directed Research and Development (LDRD) Program at Los Alamos.

References

[1] S. Li, High order central scheme on overlapping cells for magneto-hydrodynamic flows with and without constrained transport method, J. Comput. Phys. 227 (2008) 7368–7393.
[2] C.R. Evans, J.F. Hawley, Simulation of magnetohydrodynamic flows: a constrained transport method, ApJ 332 (1989) 659.
[3] D.S. Balsara, D.S. Spicer, A staggered mesh algorithm using high order Godunov fluxes to ensure solenoidal magnetic field in magnetohydrodynamics simulations, J. Comput. Phys. 149 (1999) 270–292.
[4] T.A. Gardiner, J.M. Stone, An unsplit Godunov method for ideal mhd via constrained transport, J. Comput. Phys. 205 (2005) 509–539.
[5] T.J. Barth, On the role of involutions in the discontinuous Galerkin discretization of maxwell and magneto-hydrodynamics systems, IMA Volume on Compatible Spatial Discretization, vol. 142, Springer, New York, 2006, pp. 66–88.
[6] Y. Liu, C.-W. Shu, E. Tadmor, M. Zhang, Non-oscillatory hierarchical reconstruction for central and finite-volume schemes, Commun. Comput. Phys. 2 (2007) 933–963.
[7] Y. Liu, C.-W. Shu, Z. Xu, Hierarchical reconstruction with up to second degree remainder for solving nonlinear conservation laws, Nonlinearity 22 (2009) 2799–2812.
[8] W. Dai, P.R. Woodward, A simple finite difference scheme for multidimensional magnetohydrodynamics, J. Comput. Phys. 142 (1998) 331–369.
[9] D. Ryu, F. Miniati, T.W. Jones, A. Frank, A divergence-free upwinding code for multi-dimensional mhd flows, ApJ 509 (1998) 244–255.
[10] P. Londrillo, L.D. Zanna, High-order upwinding schemes for multidimensional magnetohydrodynamics, ApJ 530 (2000) 508.
[11] G. Tóth, The $\nabla \cdot b = 0$ constraint in shock-capturing magnetohydrodynamics codes, J. Comput. Phys. 161 (2000) 605–652.
[12] Y. Liu, Central schemes on overlapping cells, J. Comput. Phys. 209 (2005) 82–104.
[13] D.S. Balsara, Divergence-free reconstruction of magnetic fields and WENO schemes for magnetohydrodynamics, 2008. Available from: arXiv:0811.2192v1.
[14] R. Spiteri, S. Tuuth, A new class of optimal high-order strong stability-preserving time discretization methods, SIAM, J. Numer. Anal. 40 (2002) 469–491.
[15] D.S. Balsara, Second order accurate schemes for magneto-hydrodynamics with divergence-free reconstruction, ApJ Suppl. 151 (2004) 149–184.
[16] M. Dumbser, D.S. Balsara, E.F. Toro, C.-D. Munz, A unified framework for the construction of one-step finite volume and discontinuous Galerkin schemes on unstructured meshes, J. Comput. Phys. 227 (2008) 8209–8253.
[17] A. Dedner, F. Kemm, D. Kröner, C.-D. Munz, T. Schnitzer, M. Wesenberg, A unified framework for the construction of one-step finite volume and discontinuous Galerkin schemes on unstructured meshes, J. Comput. Phys. 227 (2008) 8209–8253.
[18] K.G. Powell, An approximate riemann solver for MHD (that actually works in more than one dimension), Technical Report 94-24, ICASE, NASA Langley Research Center, Hampton, VA, 1994.
[19] G.S. Jiang, C.-C. Wu, A high-order WENO finite difference scheme for the equations of ideal magneto-hydrodynamics, J. Comput. Phys. 150 (1999) 561–594.
[20] F.Y. Li, C.-W. Shu, Locally divergence-free discontinuous Galerkin method for mhd equations, J. Sci. Comput. 22 (2005) 413–442.